Nanoscale

Cite this: *Nanoscale*, 2012, **4**, 4459

www.rsc.org/nanoscale

COMMUNICATION

Controlled growth of SnO_2@Fe_2O_3 double-sided nanocombs as anodes for lithium-ion batteries†

Weiwei Zhou,[a] Yee Yan Tay,[b] Xingtao Jia,[a] Denis Yu Yau Wai,[c] Jian Jiang,[a] Hng Huey Hoon[b] and Ting Yu*[acd]

Received 5th May 2012, Accepted 1st June 2012
DOI: 10.1039/c2nr31239e

A novel heterostructure is developed by grafting 1D SnO_2 nanorods onto both sides of pre-grown 2D Fe_2O_3 nanoflakes, forming a comb-like rather than tree-like branched nanostructure. The SnO_2 nanorod branches are determined to grow along the [001] direction on the (±001) planes of Fe_2O_3 nanoflakes. The resulting SnO_2@Fe_2O_3 nanocombs show stabilized cycling performance and improved volumetric energy density compared to pristine Fe_2O_3 nanoflakes presumably due to the integration of SnO_2 branches as well as the 3D hierarchical structural features.

With an ever increasing list of promising applications, there is a surge in developing efficient and scalable strategies for synthesizing nanostructures with diverse and tunable properties.[1,2] Often the recruitment of other materials with new properties to form core–shell, hetero- and/or doped structures represents a facile pathway to modify materials properties.[3–9] Heterostructures consisting of chemically distinct materials have thus attracted intense research interest due to the fact that desired properties and multifunctionality can be achieved by fine-tuning their compositions, shapes, and controlled alignments of the primary nanobuilding blocks.[5,10–13] Another key motivation underlying the preparation of heterostructures is the potential to realize the integration of nanoscale devices at a level not possible with conventional top-down methods.[14–18] As a result, architecturally assembling primary building blocks into the expected geometrical heterostructure is highly desired. Nevertheless, the complexity of the required structures and the difficulty in manipulating the entropic and/or energetic constraints of different building blocks remain formidable challenges awaiting to be resolved.

SnO_2 and Fe_2O_3, two of the most investigated functional semiconductors, have attracted great attention due to their wide range of applications in photocatalytic degradation,[19] gas sensing,[20,21] and lithium-ion batteries (LIBs).[22,23] Recent studies have revealed that the physical performances of SnO_2 or Fe_2O_3 can be remarkably improved by forming Fe_2O_3–SnO_2 heterostructures.[24–28] Especially in photocatalytic application, it is well established that by integrating α-Fe_2O_3 with SnO_2, the ease of the recombination between photogenerated holes and electrons in α-Fe_2O_3 caused by its short hole diffusion length (2–4 nm) can be effectively mitigated. This is because the photogenerated electrons in the conduction band of α-Fe_2O_3 tend to transfer to that of SnO_2 driven by the decreased potential energy.[26,28–31] So far, there are generally three kinds of, *i.e.* core–shell,[28,30,32–35] branched,[25,26,31,36,37] and random,[24,38,39] Fe_2O_3–SnO_2 heterostructures. Compared with the other two heterostructures, branched nanostructures possess two outstanding merits. One is a well-defined interface. Different from most Fe_2O_3–SnO_2 heterostructures with a simple physical contact between Fe_2O_3 and SnO_2, Fe_2O_3–SnO_2 branched heterostructures always have a definite epitaxial relationship between these two components.[25,26,31,36,37] Note that novel properties distinct from individual constituents usually stem from the interface within the heterostructure.[40,41] The other is greatly increased surface area. This is especially desirable for energy conversion and storage devices as sufficient light harvest and electrolyte infiltration can be ensured. However, regardless of the existence of diverse Fe_2O_3–SnO_2 branched heterostructures, their implementation in energy storage such as LIBs application is rarely reported.

Here, we demonstrate an integrative assembly of one-dimensional (1D) SnO_2 nanorods and two-dimensional (2D) Fe_2O_3 nanoflakes into a novel comb-like SnO_2@Fe_2O_3 branched nanostructure, in which the SnO_2 nanorods are epitaxially aligned on both sides of Fe_2O_3 nanoflakes in a high density and parallel fashion. It should be highlighted for this fabrication that: (1) the overall synthetic procedure is very simple and low cost, involving only two steps: direct heating of the Fe foil in air for the preparation of Fe_2O_3 nanoflake stems[22,42] and subsequent hydrothermal epitaxial growth of SnO_2 nanorod branches. Such a method does not contain any catalytic impurities and is capable of scaling up. More importantly, it allows the heterogeneous growth of ordered SnO_2 nanorod arrays on Fe_2O_3 nanoflakes, overcoming the potential interfacial dislocation and stretch originating from their lattice-mismatch. (2) It is the first report on using 2D Fe_2O_3 nanoflakes as the backbones to anchor 1D SnO_2 nanorod branches. The resulting comb-like nanostructure indicates the emergence of a new paradigm in branched nanostructures, in contrast to previous "tree-like" morphologies. (3) The interfacial

[a]*Division of Physics and Applied Physics, School of Physical and Mathematical Sciences, Nanyang Technological University, 21 Nanyang Link, 637371 Singapore. E-mail: yuting@ntu.edu.sg*
[b]*School of Materials Science and Engineering, Nanyang Technological University, 639798 Singapore*
[c]*Energy Research Institute@NTU (ERIAN), 50 Nanyang Drive, 637553 Singapore*
[d]*Department of Physics, Faculty of Science, National University of Singapore, 117542 Singapore*

† Electronic supplementary information (ESI) available: Experimental section, XRD and Raman patterns, SEM, TEM, and optical images. See DOI: 10.1039/c2nr31239e

orientation relationship between Fe_2O_3 and SnO_2 is preliminarily determined to be $(001)_{SnO_2}//(001)_{Fe_2O_3}$, different from previously reported SnO_2–Fe_2O_3 branched heterostructures.[25,26,31,36,37] This is essential for fundamental studies of the crystallographic link between Fe_2O_3 and SnO_2. (4) The as-obtained SnO_2@Fe_2O_3 comb-like branched heterostructures are freestanding on conductive substrates (*e.g.*, Fe foil). It should be noted that few reports are available on preparing self-supported Fe_2O_3–SnO_2 heterostructures till now,[29,43] let alone branched heterostructures.[25] As aforementioned, SnO_2–Fe_2O_3 branched heterostructures are hardly ever reported for LIBs application except for our previous attempt on studying the electrochemical lithium storage performances of the reverse status, *i.e.* Fe_2O_3 on SnO_2 branched nanostructures.[25] Herein, given the high lithium storage capacities of both SnO_2 and Fe_2O_3 and the freestanding feature of the resulting SnO_2@Fe_2O_3 nanocombs, the yielding composites are further exploited as anodes for LIBs application. The significance in using such heterostructures for LIBs can be stressed as follows. This unique freestanding hybrid architecture can: (1) completely obviate the need for any ancillary additives such as carbon black and polymer binder; (2) show enhanced reversible capacity and cycling performance compared to pristine Fe_2O_3, which is due both to the prior integration with SnO_2 that can offer high capacity by electrochemically alloying with Li and the large electrode–electrolyte contact area; and (3) alleviate the inferior packing problems associated with nanostructures owing to the improved compactness.

Fig. 1a shows the optical images captured during the process flow for the synthesis of SnO_2@Fe_2O_3 heterostructures. The Fe foil is first polished, cleaned, and then annealed at 400 °C, enabling the growth of Fe_2O_3 nanoflakes. X-ray diffraction (XRD) and Raman spectroscopy measurements show that two phases, Fe_2O_3 and Fe_3O_4, coexist in the sample obtained at this stage (Fig. S1†), which is consistent with our previous results.[42] The signals of Fe_3O_4 are from a condensed Fe_3O_4 layer formed on top of the Fe foil, acting as the precursor for the growth of Fe_2O_3 nanoflakes. An obvious color change can be viewed before and after annealing. Although eventual hydrothermal growth of SnO_2 branches does not lead to visible alteration in color, the branched nanostructures are indeed formed. Scanning electron microscopy (SEM) images exhibit the evolution from Fe_2O_3 nanoflakes to SnO_2@Fe_2O_3 nanocombs (Fig. 1b and c). Interestingly, pristine Fe_2O_3 nanoflakes exhibit very similar morphologies to the grass (Fig. 1b and its inset). They are smooth and of the thickness of ~10 nm, having a non-constant planar width in the range of *ca.* 60–300 nm (Fig. 1b). After branching with SnO_2, the hierarchical SnO_2@Fe_2O_3 nanostructures look quite like dog's tail grasses, possessing fuzzy surfaces (Fig. 1c and its inset). Further close observations from the SEM images show that SnO_2 branches emanate from both sides of Fe_2O_3 nanoflake backbones and are arranged regularly and parallel to each other on each side, forming an intriguing double-sided comb-like structure (Fig. 1d and e). Albeit with dense coverage of SnO_2 nanorods on both sides, the edges of Fe_2O_3 nanoflakes remain exposed. The average length and diameter of the secondary SnO_2 nanorods are measured to be *ca.* 150 nm and 20 nm, respectively.

Detailed microstructures and compositions of these 3D branched nanostructures are further characterized by transmission electron microscopy (TEM). It is extremely difficult to analyze the epitaxial relationship from the lateral view of the heterostructures due to the large, varying planar dimension of these SnO_2@Fe_2O_3 hierarchical nanostructures. Consequently, we investigate the Fe_2O_3 stem and the SnO_2 branch individually and thereby determine their potential epitaxial relationship. Fig. 2a presents the high-resolution TEM (HRTEM) image of a Fe_2O_3 nanoflake, showing three groups of parallel fringes with the same *d*-spacing of 0.25 nm. Combining with the corresponding Fast-Fourier Transformation (FFT) pattern taken

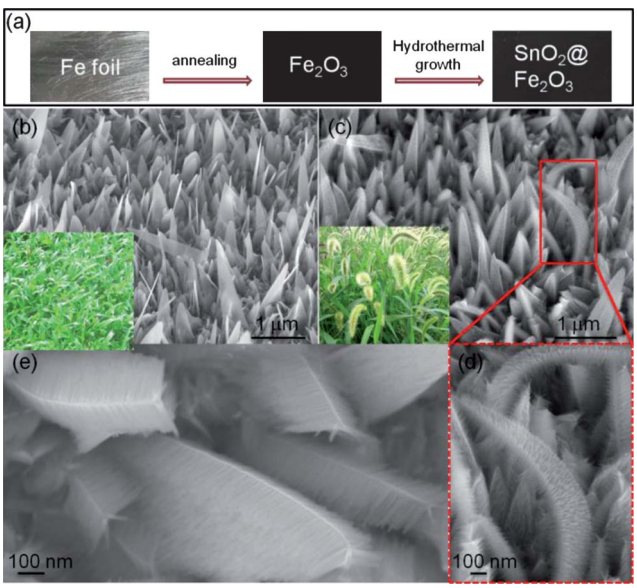

Fig. 1 (a) Optical images of the samples captured during the process flow. Typical SEM images of (b) Fe_2O_3 nanoflakes and (c) SnO_2@Fe_2O_3 heterostructures. Insets in (b) and (c) are the photo images of grass and dog's tail grass, respectively. (d and e) High-magnification SEM images of SnO_2@Fe_2O_3 heterostructures.

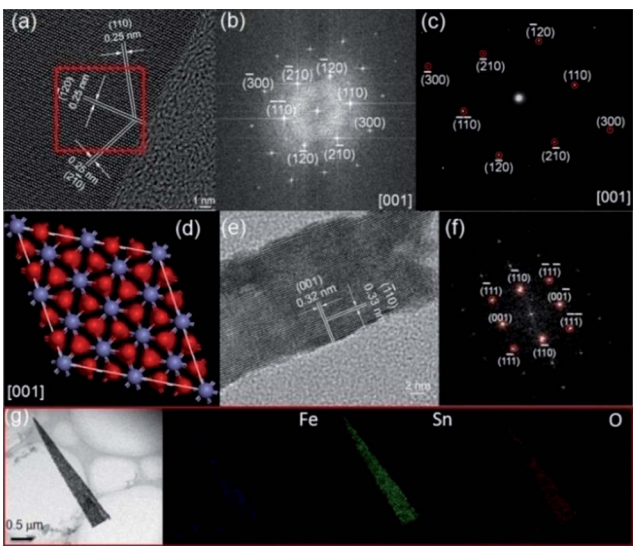

Fig. 2 (a) HRTEM image, (b) FFT pattern taken from the rectangular area in (a), and (c) corresponding SAED pattern of a Fe_2O_3 nanoflake. (d) Crystal structure of Fe_2O_3 along the [001] zone axis. (e) HRTEM image and (f) corresponding SAED pattern of a SnO_2 nanorod separated from a SnO_2@Fe_2O_3 nanocomb *via* sonication. (g) TEM image and corresponding EDX elemental mappings of Fe, Sn, and O for a SnO_2@Fe_2O_3 nanocomb, showing the uniform distribution of each element.

from the rectangular area in Fig. 2a (Fig. 2b), the crystalline planes in the HRTEM image can be indexed to $(\bar{1}20)$, $(\bar{2}10)$, and (110) planes of rhombohedral Fe_2O_3, respectively. Besides, it can be observed that the FFT pattern is in high consistence with the selected area electron diffraction (SAED) pattern (Fig. 2c), which can be indexed in accord with the [001] zone axis of rhombohedral Fe_2O_3 (Fig. 2d). Thermodynamically, the nanoflakes tend to lay their basal plane on the TEM grid with a fully coated carbon film. The [001] zone axis is observed with several of the nanoflakes with minimal tilting of the samples. Therefore, it can be unambiguously deduced that the exposed surfaces of Fe_2O_3 nanoflakes are (±001) planes, acting as the substrates for the epitaxial growth of secondary branches. Fig. 2e shows the HRTEM image of a SnO_2 nanorod. Similarly, in combination with the corresponding SAED pattern (Fig. 2f), the marked interplanar *d*-spacings of 0.32 nm and 0.33 nm correspond to the (001) and $(\bar{1}10)$ lattice fringes of tetragonal SnO_2, respectively. The SnO_2 nanorod can be determined to grow along the [001] direction. The TEM analyses suggest that the SnO_2 nanorods prefer to branch perpendicularly on the Fe_2O_3 nanoflakes such that the SnO_2 branches epitaxially grow along the [001] direction on the (±001) planes of Fe_2O_3 nanoflakes, forming a $(001)_{SnO_2}/(001)_{Fe_2O_3}$ interface. The composition of the single SnO_2@Fe_2O_3 nanocomb is further identified by energy-dispersive X-ray spectroscopy (EDX) mapping. It can be seen that the Fe, Sn, and O signals appear all over the whole structure, showing exactly the same shape as observed under TEM (Fig. 2g). Notably, the SnO_2 nanorods are tightly adhered onto the surface of Fe_2O_3 nanoflakes even after 0.5 h sonication (Fig. S2†). This tough structural integrity is highly desirable for energy storage devices that require the active materials can endure repeated cycling processes.

In order to shed light on the evolution process of such a branched nanostructure, samples obtained at different reaction durations were characterized. As shown in Fig. 3a, after the initial 1 h of growth, no visible change occurred in pristine Fe_2O_3 nanoflakes, whose surfaces remained clean and smooth as before. However, small dot- and needle-shaped nuclei appeared on both sides of Fe_2O_3 nanoflakes 1 h later (Fig. 3b and S3†). Subsequent growth to 3 h led to the formation of double-sided comb-like SnO_2@Fe_2O_3 nanostructures (Fig. 3c). Further prolonging the growth time only induced the diameter increase of SnO_2 nanorods (Fig. 3d). The synthesis and branching process of the SnO_2@Fe_2O_3 hierarchical nanostructures is schematically illustrated for better understanding (Fig. 3e), consisting basically of three steps. Firstly, the Fe_2O_3 nanoflakes are grown on the Fe foil through a possible solid–liquid–solid (SLS) mechanism that we proposed previously.[31] Secondly, the SnO_2 nanoparticles heteronucleate through dehydration of $Sn(OH)_6^{2-}$, followed by epitaxial growth on the surfaces of Fe_2O_3 nanoflakes, establishing the $(001)_{SnO_2}/(001)_{Fe_2O_3}$ interfaces. Finally, these particles anisotropically grow up into aligned nanorod arrays on both sides of Fe_2O_3 nanoflakes along the [001] direction, resulting in the 2-fold symmetrically branched SnO_2@Fe_2O_3 nanostructures.

As far as LIBs are concerned, the use of nanomaterials is highly beneficial for improving the capacities and rate capabilities of solid-state electrodes due to the small diffusion lengths and large surface areas. Nevertheless, only those freestanding nanostructures directly grown onto a plane current collector, completely precluding the need for ancillaries and further processing, can well maintain the gains in diffusion length and electronic conductivity associated with the reduced active material size. Meanwhile, the addition of

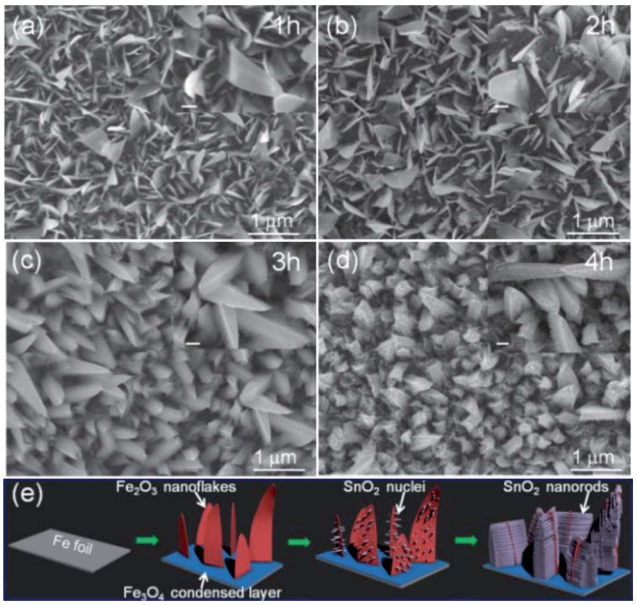

Fig. 3 SEM images of the products obtained at different reaction stages: (a) 1 h; (b) 2 h; (c) 3 h; and (d) 4 h. The insets are corresponding high-magnification SEM images. The scale bars in the insets are 200 nm. (e) Schematic illustration of the formation process of hierarchically assembled SnO_2@Fe_2O_3 nanocombs.

supplementary interfaces (current collector–active materials, active material–active material, active material–binder, *etc.*) can also be avoided. Recently, the use of composites is a very important study in finding a solution to the problem of the large capacity fading; therefore we intend to employ our resultant self-supported SnO_2@Fe_2O_3 heterostructures directly as a working electrode, aiming at achieving improved performances.

The performances of the bare Fe_2O_3 nanoflakes and SnO_2@Fe_2O_3 nanocombs as the anodes of LIBs were tested by galvanostatic discharge–charge and cyclic voltammetry (CV) measurements. The preparation of these working electrodes can be accomplished simply by cutting the Fe-foil supported nanostructures into small platelets without further processing (Fig. S4†). As expected, the nano-architectured SnO_2@Fe_2O_3 electrode manifests superior reversibility and cycling stability towards pristine Fe_2O_3 nanoflakes (Fig. 4). As shown in Fig. 4a, the SnO_2@Fe_2O_3 nanocombs deliver a stable areal capacity with an average value of 0.43 mA h cm^{-2} up to150 cycles after initial fast capacity fading, which is about 1.7 times of that for bare Fe_2O_3 nanoflakes (0.25 mA h cm^{-2}). The coulombic efficiency of the composite electrode is also slightly improved, which is likely due to the synergetic effect between these two components. For example, the presence of Fe nanoparticles generated from the lithiation process of the inner Fe_2O_3 core can promote the reversibility of the reaction between SnO_2 and Li^+.[27] In addition, despite the severe capacity degradation in the first 10 cycles, the SnO_2@Fe_2O_3 heterostructures can always deliver twice the areal capacities of that for Fe_2O_3 nanoflakes under different current densities (Fig. 4b). Noticeably, both electrodes can exhibit high areal capacity again when the current density is lowered back to 0.18 mA cm^{-2}. The slightly reduced charge transfer resistance (23.6 Ω) for the composite electrode towards bare Fe_2O_3 nanoflakes (29.6 Ω) partially accounts for the high capacity at different current rates (inset in Fig. 4b). Fig. 4c and d depict the

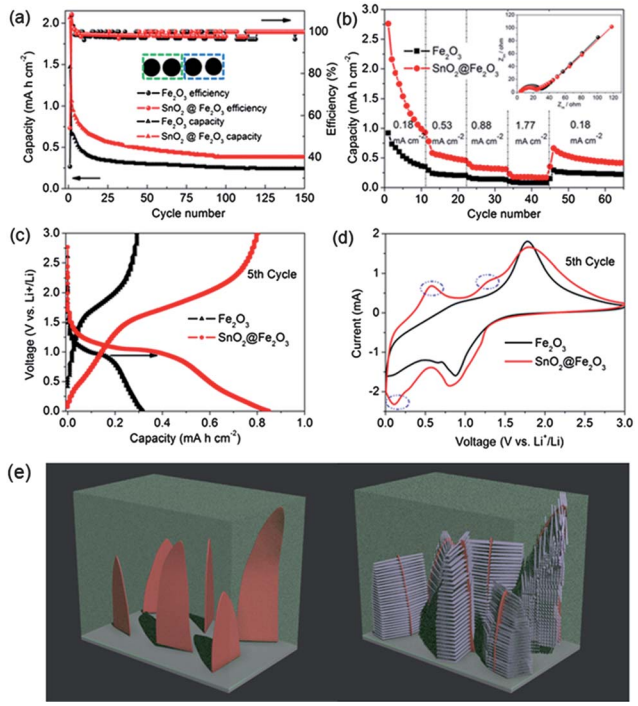

Fig. 4 (a) Cycling behavior and coulombic efficiency of SnO_2@Fe_2O_3 heterostructures and Fe_2O_3 nanoflakes under a current density of 0.18 mA h cm^{-2} for 150 cycles. The inset shows the optical images of the SnO_2@Fe_2O_3 (right two) and Fe_2O_3 (left two) platelets as working electrodes. (b) Comparison of the rate capabilities of SnO_2@Fe_2O_3 heterostructures and Fe_2O_3 nanoflakes cycled under different current densities. The inset shows their respective Nyquist plots. (c) Voltage profiles for SnO_2@Fe_2O_3 and Fe_2O_3 electrodes during the 5th cycle under a current density of 0.18 mA h cm^{-2}. The arrow indicates the prolonged plateau for SnO_2@Fe_2O_3 during the discharge process. (d) CV curves for SnO_2@Fe_2O_3 and Fe_2O_3 electrodes during the 5th cycle at a scan rate of 0.5 mV s^{-1}. The presence of the peaks marked by the blue dashed circles is due to the redox reactions between SnO_2 and Li^+. (e) Schematic illustration of the improved occupation of the SnO_2@Fe_2O_3 nanocombs within a certain volume, thereby establishing high volumetric energy density.

charge–discharge and CV curves of SnO_2@Fe_2O_3 and Fe_2O_3 during the 5th cycle, respectively. A long plateau during the charge–discharge process and an enlarged area surrounding the CV curve can be clearly observed for the SnO_2@Fe_2O_3, which indicate straightforwardly the superior performances of the composite electrode. While the introduction of SnO_2 definitely contributes to the enhanced capacity of the composite electrode by providing more active materials that can electrochemically alloy with Li, the unique 3D comb-like morphologies are considered to play a crucial role in the capacity improvement as well. Branching the SnO_2 nanorods on both sides of Fe_2O_3 nanoflakes rather than growing them on a plane substrate can induce largely increased surface area and simultaneously give rise to the loose arrangement of SnO_2 nanorods, allowing sufficient electrolyte infiltration and the subsequent enhancement of electrode–electrolyte contact area. Although the specific capacity of the electrode cannot be determined due to the uncertainty of the mass of active materials, the volumetric energy density of the composite electrode is certainly improved. This is because the introduction of SnO_2 branches does not change the initial volume occupied by the bare Fe_2O_3 nanoflakes but fills the free spaces between the Fe_2O_3 nanoflakes, resulting in a more dense structure (Fig. 4e). In this case, the improved areal capacity will undoubtedly lead to the enhanced volumetric energy density. It is important to highlight that the lower volumetric energy density is one of the disadvantages that concomitantly appears when nanomaterials are used as the electrodes for LIBs due to the inferior packing of particles. It is even more difficult to improve the volumetric energy densities for those freestanding nanostructures as other materials are difficult to be added without destroying their structures. When such a situation arises, preparation of composites at the nanoscale is highly important.

In summary, we have demonstrated a novel comb-like branched heterostructure by hydrothermally grafting 1D SnO_2 nanorods onto both sides of pre-grown 2D Fe_2O_3 nanoflakes. The secondary SnO_2 nanorods are determined to grow on the ($\pm$001) planes of Fe_2O_3 nanoflakes along the [001] direction, accounting for the unique 2-fold symmetrical growth. The resulting SnO_2@Fe_2O_3 nanocombs show stabilized cycling performance and improved volumetric energy density compared to pristine Fe_2O_3 nanoflakes, which are presumably due to the integration of SnO_2 branches as well as the 3D hierarchical structural features. We believe such a novel comb-like SnO_2@Fe_2O_3 heterostructure is also a promising candidate in photocatalytic, water splitting, and photovoltaic applications.

Acknowledgements

This work is supported by the Singapore National Research Foundation under NRF RF award no. NRF-RF2010-07 and MOE Tier 2 MOE2009-T2-1-037.

Notes and references

1 X. Duan, C. Niu, V. Sahi, J. Chen, J. W. Parce, S. Empedocles and J. L. Goldman, *Nature*, 2003, **425**, 274–278.
2 A. S. Arico, P. Bruce, B. Scrosati, J.-M. Tarascon and W. van Schalkwijk, *Nat. Mater.*, 2005, **4**, 366–377.
3 Y. Wu, J. Xiang, C. Yang, W. Lu and C. M. Lieber, *Nature*, 2004, **430**, 61–65.
4 S. Zhou, X. Liu and D. Wang, *Nano Lett.*, 2010, **10**, 860–863.
5 X.-L. Yu, J.-G. Song, Y.-S. Fu, Y. Xie, X. Song, J. Sun and X.-W. Du, *J. Phys. Chem. C*, 2010, **114**, 2380–2384.
6 Y. Baek, Y. Song and K. Yong, *Adv. Mater.*, 2006, **18**, 3105–3110.
7 Y. Lin, S. Zhou, X. Liu, S. Sheehan and D. Wang, *J. Am. Chem. Soc.*, 2009, **131**, 2772–2773.
8 W. Zhou, J. Zhu, C. Cheng, J. Liu, H. Yang, C. Cong, C. Guan, X. Jia, H. J. Fan, Q. Yan, C. M. Li and T. Yu, *Energy Environ. Sci.*, 2011, **4**, 4954–4961.
9 Y. He, X. Yu, Y. Wang, H. Li and X. Huang, *Adv. Mater.*, 2011, **23**, 4938–4941.
10 C. Cheng, B. Liu, H. Yang, W. Zhou, L. Sun, R. Chen, S. F. Yu, J. Zhang, H. Gong, H. Sun and H. J. Fan, *ACS Nano*, 2009, **3**, 3069–3076.
11 U. K. Gautam, X. Fang, Y. Bando, J. Zhan and D. Golberg, *ACS Nano*, 2008, **2**, 1015–1021.
12 K. Evanoff, A. Magasinski, J. Yang and G. Yushin, *Adv. Energy Mater.*, 2011, **1**, 495–498.
13 Y. Q. Zou and Y. Wang, *ACS Nano*, 2011, **5**, 8108–8114.
14 P. L. Taberna, S. Mitra, P. Poizot, P. Simon and J. M. Tarascon, *Nat. Mater.*, 2006, **5**, 567–573.
15 F.-F. Cao, J.-W. Deng, S. Xin, H.-X. Ji, O. G. Schmidt, L.-J. Wan and Y.-G. Guo, *Adv. Mater.*, 2011, **23**, 4415–4420.
16 J. Liu, J. Jiang, C. Cheng, H. Li, J. Zhang, H. Gong and H. J. Fan, *Adv. Mater.*, 2011, **23**, 2075–2080.
17 K. Sun, Y. Jing, N. Park, C. Li, Y. Bando and D. Wang, *J. Am. Chem. Soc.*, 2010, **132**, 15465–15467.
18 K. A. Dick, K. Deppert, M. W. Larsson, T. Martensson, W. Seifert, L. R. Wallenberg and L. Samuelson, *Nat. Mater.*, 2004, **3**, 380–384.

19 H. Xie, Y. Z. Li, S. F. Jin, J. J. Han and X. J. Zhao, *J. Phys. Chem. C*, 2010, **114**, 9706–9712.
20 J. Ming, Y. Q. Wu, L. Y. Wang, Y. C. Yu and F. Y. Zhao, *J. Mater. Chem.*, 2011, **21**, 17776–17782.
21 H. Chen, Z. Y. Liu and G. Fu, *Sens. Actuators, B*, 2011, **156**, 912–917.
22 M. V. Reddy, T. Yu, C. H. Sow, Z. X. Shen, C. T. Lim, G. V. Subba Rao and B. V. R. Chowdari, *Adv. Funct. Mater.*, 2007, **17**, 2792–2799.
23 X. W. Lou, Y. Wang, C. Yuan, J. Y. Lee and L. A. Archer, *Adv. Mater.*, 2006, **18**, 2325–2329.
24 V. V. Kovalenko, M. N. Rumyantseva, A. M. Gaskov, E. V. Makshina, V. V. Yushchenko, I. I. Ivanova, A. Ponzoni, G. Faglia and E. Comini, *Inorg. Mater.*, 2006, **42**, 1088–1093.
25 W. Zhou, C. Cheng, J. Liu, Y. Y. Tay, J. Jiang, X. Jia, J. Zhang, H. Gong, H. H. Hng, T. Yu and H. J. Fan, *Adv. Funct. Mater.*, 2011, **21**, 2439–2445.
26 M. Niu, F. Huang, L. Cui, P. Huang, Y. Yu and Y. Wang, *ACS Nano*, 2010, **4**, 681–688.
27 J. S. Chen, C. M. Li, W. W. Zhou, Q. Y. Yan, L. A. Archer and X. W. Lou, *Nanoscale*, 2009, **1**, 280–285.
28 W. Wu, S. F. Zhang, F. Ren, X. H. Xiao, J. Zhou and C. Z. Jiang, *Nanoscale*, 2011, **3**, 4676–4684.
29 J. Kang, Q. Kuang, Z.-X. Xie and L.-S. Zheng, *J. Phys. Chem. C*, 2011, **115**, 7874–7879.
30 L. P. Zhu, N. C. Bing, D. D. Yang, Y. Yang, G. H. Liao and L. J. Wang, *CrystEngComm*, 2011, **13**, 4486–4490.
31 J. Xu, F. Huang, Y. L. Yu, A. P. Yang and Y. S. Wang, *CrystEngComm*, 2011, **13**, 4873–4877.
32 X. W. Lou, C. L. Yuan and L. A. Archer, *Adv. Mater.*, 2007, **19**, 3328–3332.
33 Y. J. Chen, C. L. Zhu, L. J. Wang, P. Gao, M. S. Cao and X. L. Shi, *Nanotechnology*, 2009, **20**, 045502 (6pp).
34 J. S. Chen, C. M. Li, W. W. Zhou, Q. Y. Yan, L. A. Archer and X. W. Lou, *Nanoscale*, 2009, **1**, 280–285.
35 J. Lu, D. W. Qi, C. H. Deng, X. M. Zhang and P. Y. Yang, *Nanoscale*, 2010, **2**, 1892–1900.
36 D.-F. Zhang, L.-D. Sun, C.-J. Jia, Z.-G. Yan, L.-P. You and C.-H. Yan, *J. Am. Chem. Soc.*, 2005, **127**, 13492–13493.
37 M. Niu, Y. Cheng, Y. Wang, L. Cui, F. Bao and L. Zhou, *Cryst. Growth Des.*, 2008, **8**, 1727–1729.
38 H. Uchiyama, M. Yukizawa and H. Kozuka, *J. Phys. Chem. C*, 2011, **115**, 7050–7055.
39 M. B. Sahana, C. Sudakar, G. Setzler, A. Dixit, J. S. Thakur, G. Lawes, R. Naik, V. M. Naik and P. P. Vaishnava, *Appl. Phys. Lett.*, 2008, **93**, 231909.
40 D. J. Milliron, S. M. Hughes, Y. Cui, L. Manna, J. Li, L.-W. Wang and A. P. Alivisatos, *Nature*, 2004, **430**, 190–195.
41 Q. Kuang, Z.-Y. Jiang, Z.-X. Xie, S.-C. Lin, Z.-W. Lin, S.-Y. Xie, R.-B. Huang and L.-S. Zheng, *J. Am. Chem. Soc.*, 2005, **127**, 11777–11784.
42 T. Yu, Y. Zhu, X. Xu, K.-S. Yeong, Z. Shen, P. Chen, C.-T. Lim, J. T.-L. Thong and C.-H. Sow, *Small*, 2006, **2**, 80–84.
43 W. Q. Zeng, F. P. Zheng, R. Z. Li, Y. Zhan, Y. Y. Li and J. P. Liu, *Nanoscale*, 2012, **4**, 2760–2765.